Glass-Based Transparent Conductive Electrode: Its Application to Visible-to-Ultraviolet Light-Emitting Diodes

Tae Ho Lee,[†] Kyeong Heon Kim,[†] Byeong Ryong Lee,[†] Ju Hyun Park,[†] E. Fred Schubert,[‡] and Tae Geun Kim*,[†]

[†]School of Electrical Engineering, Korea University, Anam-dong 5-ga, Seongbuk-gu, Seoul 136-701, Republic of Korea

[‡]Department of Electrical Computer and Systems Engineering, Rensselaer Polytechnic Institute, 110 Eighth Street, Troy, New York 12180, United States

S *Supporting Information*

ABSTRACT: Nitride-based ultraviolet light-emitting diodes (UV LEDs) are promising replacements for conventional UV lamps. However, the external quantum efficiency of UV LEDs is much lower than for visible LEDs due to light absorption in the p-GaN contact and electrode layers, along with p-AlGaN growth and doping issues. To minimize such absorption, we should obtain direct ohmic contact to p-AlGaN using UV-transparent ohmic electrodes and not use p-GaN as a contact layer. Here, we propose a glass-based transparent conductive electrode (TCE) produced using electrical breakdown (EBD) of an AlN thin film, and we apply the thin film to four (Al)GaN-based visible and UV LEDs with thin buffer layers for current spreading and damage protection. Compared to LEDs with optimal ITO contacts, our LEDs with AlN TCEs exhibit a lower forward voltage, higher light output power, and brighter light emission for all samples. The ohmic transport mechanism for current injection and spreading from the metal electrode to p-(Al)GaN layer via AlN TCE is also investigated by analyzing the p-(Al)GaN surface before and after EBD.

KEYWORDS: light-emitting diode, conducting filament, transparent conductive electrode, wide-bandgap, ultraviolet
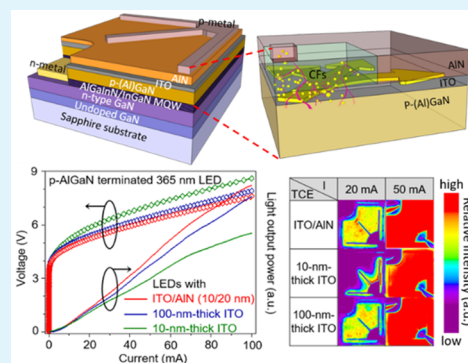
1. INTRODUCTION

The transparent conductive electrode (TCE) is one of the key components that can improve the performance of various optoelectronic devices including light-emitting diodes (LEDs),[1−3] organic LEDs,[4−7] and solar cells.[8−13] On the basis of Maxwell's equations, high electrical conductivity, and high optical transparency are mutually exclusive properties, thereby making it difficult to develop materials with high conductivity and transparency. Currently, indium-doped tin oxide (ITO) is most widely used as a TCE in the visible (VIS) region;[3] however, it has a fundamental limit owing to indium's increasing cost and the unavailability of transparency in the ultraviolet (UV) wavelength band.[14−17] Therefore, much attention is being paid to new types of TCEs, which are cost-effective and highly transparent in broad spectral ranges from VIS to UV. Some groups reported metal nanowires,[11,18−21] metal nano-meshes,[22−24] graphene,[2,4,5,10,25−27] carbon nanotubes,[8,28,29] metal-oxides,[1,13,30] and conductive polymers,[6,10,31] as replacements for (or alternatives to) conventional ITO. However, all of these efforts are still under way to overcome the well-known trade-off between optical transmittance and electrical conductivity.

Recently, a universal method of producing TCEs using wide-bandgap (WB) materials such as silicon oxides and nitrides has been reported.[32] Interestingly, these glass-based TCEs (G-TCEs) enable effective current injection from a metal to a WB semiconductor such as p-AlGaN under biases, via conducting filaments (CFs) formed by electrical breakdown (EBD) in the G-TCE, while maintaining high transmittance even in the deep UV region (>95% at 280 nm). Using this novel method, we can make a direct ohmic contact to lightly doped p-AlGaN layers for UV LEDs, particularly with UV-transparent G-TCEs. Note that it is known to be quite difficult to obtain ohmic behavior directly on p-AlGaN using conventional ohmic methods because its work functionis much greater than that of a contact metal; furthermore, shallow acceptor dopants for p-AlGaN are not available. However, in the course of device applications, some issues related to either partial damage in the multiple-quantum well (MQW) during the EBD process and insufficient current spreading into the p-AlGaN layer via G-TCE were observed, particularly in lateral-type LEDs (Figure S1). These issues should be resolved before making usage of the G-TCE in various areas of optoelectronics including LEDs.

In this study, we propose a G-TCE using an AlN thin film, and apply it to (Al)GaN LEDs as a p-type electrode with a thin ITO buffer layer below the AlN, in the form of ITO/AlN TCE, for
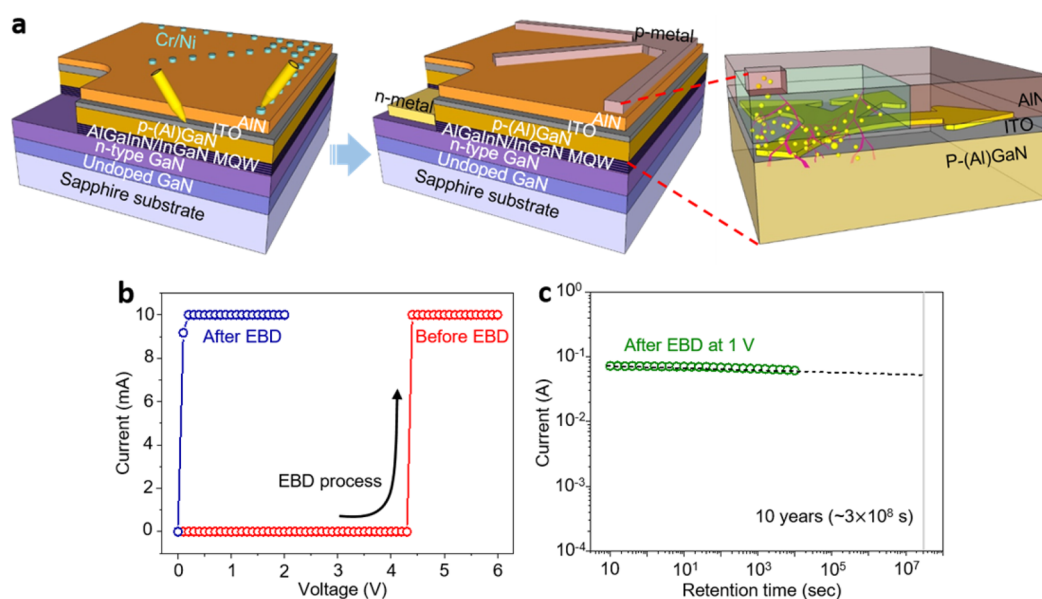
Figure 1. Schematic illustrations of the proposed (Al)GaN LED with ITO/AlN (10/20 nm) TCE. (a) Schematic view of lateral-type (Al)GaN LED with ITO/AlN TCE after the EBD. Tripod-shaped metal pads (Cr/Ni), under which 55 metal dots exist to form the CFs using the EBD process, are designed to observe the current spreading effect. The magnified image on the right-hand side shows that current can be injected via the CFs formed in the AlN layer after the EBD, and spread out via thin ITO buffer layers. (b) Current−voltage characteristics measured for ITO/AlN TCE, before (red open circles) and after (blue open circles) the EBD, deposited on the p-GaN terminated 385 nm wafer. The EBD voltage is observed at ~4 V. (c) Long-term stability of the LRS current at 1 V for the ITO/AlN TCE after the EBD deposited on the p-GaN terminated 385 nm wafer.

both effective current spreading and MQW damage prevention during the EBD process. Here, a 10 nm thick ITO was selected as the buffer layer based on the measured sheet resistance and optical transmittance versus ITO thickness (Figure S2). Moreover, we chose a 20 nm thick AlN film as a contact electrode among the five G-TCEs (ZnO, Si_3N_4, AlN, Al_2O_3, SiO_2) because it exhibited a relatively lower EBD voltage ($V_{EBD} \approx$ 4 V on p-GaN) and higher transmittance (~95% at 365 nm on quartz substrates) due to its larger bandgap energy (~6 eV) compared to other G-TCEs, as shown in Figure 1b and Figure S3, respectively. Note that the V_{EBD} of ZnO was slightly lower than that of AlN, but its transmittance (or energy bandgap) was much lower (smaller) than that of AlN. The VEBD values for the other three G-TCEs were measured to be in the range of 11−16 V. We also examined the effect of the AlN thickness (20, 40, 60 nm) on the LED performance, but the EBD voltage just increased without any gain in the optical performance. We then applied ITO/AlN (10/20 nm) TCEs to four different types of LEDs (p-GaN terminated 450 nm wafer, p-GaN terminated 385 nm wafer, p-$Al_{0.05}Ga_{0.95}$N terminated 385 nm wafer, and p-$Al_{0.1}Ga_{0.9}$N terminated 365 nm wafer; Scheme S1) to verify the validity of our ohmic method at the device level.

2. RESULTS AND DISCUSSION

Figure 1a shows schematic overviews of lateral-type (Al)GaN LEDs with ITO/AlN TCEs. Here, the thicknesses of ITO and AlN layers measured by AFM were 10 and 20 nm, respectively (Figure S4). A tripod-shaped p-metal pad (Cr/Ni), which had 55 metal dots that are located under it, to form the CFs (or current injection path) during the EBD process, was specially designed to easily observe the current spreading effect under a low-current operation. The magnified figure on the right-hand side of Figure 1a shows that the current can be injected via the CFs formed in the AlN TCE after the EBD, and spread out via thin ITO buffer

layers. A detailed fabrication process for (Al)GaN LEDs with ITO/AlN TCEs is presented in Scheme S2.

We measured the current−voltage (I−V) curves of ITO/AlN TCEs deposited on four LED wafers before (red open circles) and after (blue open circles) the EBD (Figure 1b and Figure S5). The EBD process was performed in the air at room temperature, where the direct current (DC) voltage was swept from 0−6 V with a ramp rate of 0.1 V per second using a two-point probe contact between the metal pad (Cr/Ni) and ITO buffer layer to form the CFs in the ITO/AlN TCE. Initially, the TCE was maintained at high resistance state (HRS); however, a steep increase in the current level was observed at ~4 V (V_{EBD}). A compliance current of 10 mA was imposed to prevent any damage to the device. Then, in the second DC voltage sweep, the current level increased linearly and reached a maximum compliance current (10 mA) even below 0.5 V. This abrupt transition from HRS to low-resistance state (LRS) is the result of the CF formation in the ITO/AlN TCE, where the current level after the EBD increased from a few pA to ~100 mA even at 1 V. We also measured the retention of the LRS at 1 V, and extrapolated the result against the delay time (Figure 1c) to evaluate the long-term stability of the LRS. It has been confirmed that the LRS can be maintained up to ten years.

We measured the typical I−V curves for different transmission line model (TLM) contact spacings of the ITO/AlN (10/20 nm) TCEs before and after the EBD, and the reference ITO layers were deposited on the p-GaN terminated 450 nm wafer, p-GaN terminated 385 nm wafer, p-AlGaN terminated 385 nm wafer, and p-AlGaN terminated 365 nm wafer. Before the EBD, almost no current flow was observed for all four samples, due to the insulating properties of AlN; however, AlN-based TCEs exhibited excellent ohmic behavior for all four samples after the EBD in the range of ±1 V, as shown in Figure 2a−d. We also plotted the I−V curves for the reference ITOs for comparison (Figure S6). The thickness of the reference ITO was carefully
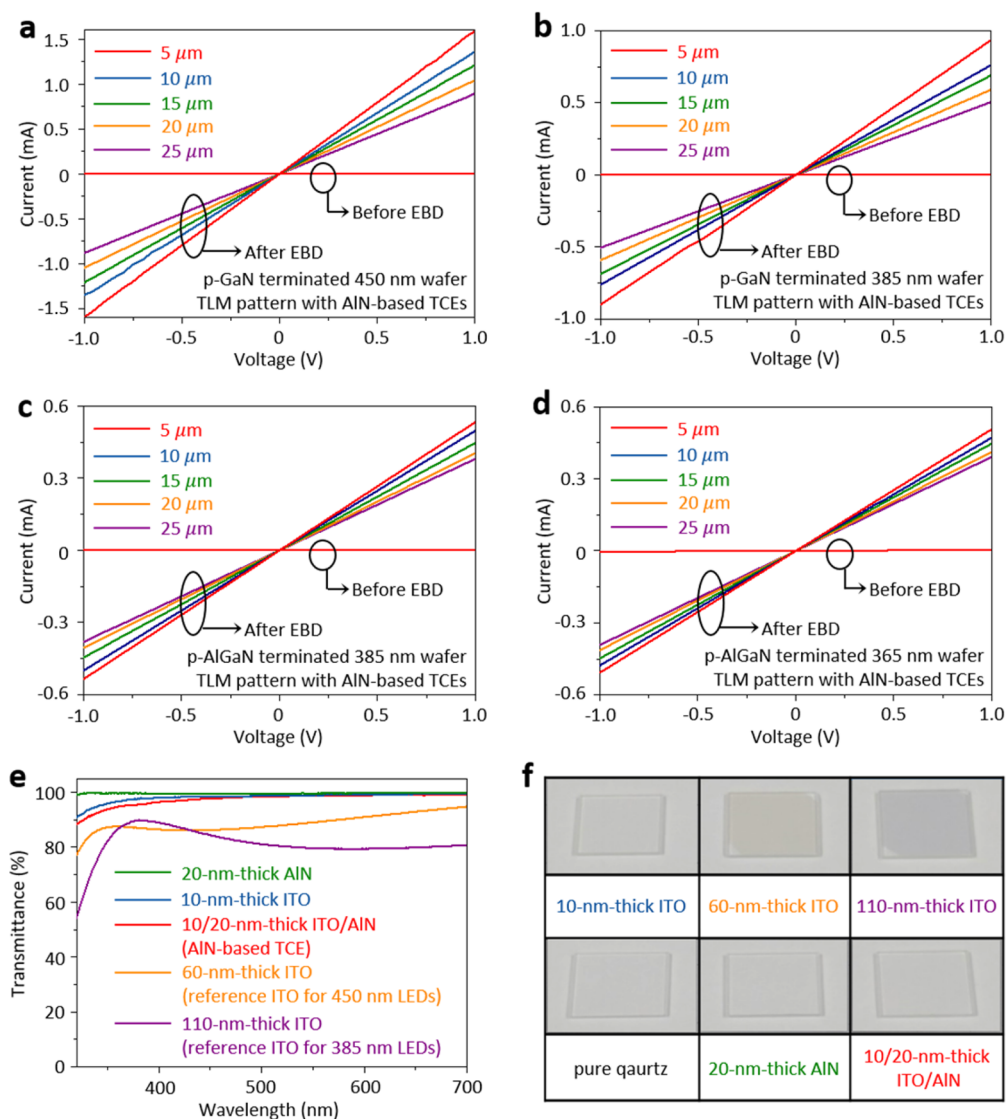
Figure 2. Ohmic behavior of (Al)GaN LEDs and optical transmittance. Typical current−voltage characteristics measured for different contact spacings (TLM pattern) of the ITO/AlN TCEs, before and after the EBD process, deposited on (a) p-GaN terminated 450 nm wafer, (b) p-GaN terminated 385 nm wafer, (c) p-AlGaN terminated 385 nm wafer, and (d) p-AlGaN terminated 365 nm wafer, respectively. (e) Transmission spectra measured for 20 nm thick AlN (green line), 10 nm thick ITO (blue line), 10/20 nm thick ITO/AlN (proposed AlN-based TCE, red line), 60 nm thick ITO (reference ITO for 450 nm LED, orange line), 110 nm thick ITO (reference ITO for 385 nm LED, purple line) deposited on the quartz substrates. (f) Photographs of each sample placed onto a white-colored background.

Table 1. Performance Parameters for the Fabricated LEDs. Forward Voltage (V_F), Reverse Leakage Current (I_L), Light Output Power (P_O), Specific Contact Resistance (ρ_C), and Transmittance

wafers	samples	V_F at 20 mA (V)	I_L at 10 V (nA)	P_O at 100 mA (a.u.)	ρ_C (Ω cm^2)	transmittance (%)
p-GaN terminated 450 nm LED	ITO/AlN (10/20 nm)	3.2 (0%)	−31.5	129.4 (1.5% ↑)	3.3×10^{-3}	97.8 at 450 nm
	60 nm thick ITO	3.2	−33.5	127.5	3.4×10^{-3}	86.3 at 450 nm
p-GaN terminated 385 nm LED	ITO/AlN (10/20 nm)	3.45 (4.2% ↓)	−2.6	74.4 (4.7% ↑)	5.6×10^{-3}	95.7 at 385 nm
	110 nm thick ITO	3.6	−3.6	71.0	7.2×10^{-3}	89.7 at 385 nm
p-AlGaN terminated 385 nm LED	ITO/AlN (10/20 nm)	4.4 (6.4% ↓)	−11.4	63.5 (13.0% ↑)	1.9×10^{-2}	95.7 at 385 nm
	110 nm thick ITO	4.7	−13.7	56.2	2.5×10^{-2}	89.7 at 385 nm
p-AlGaN terminated 365 nm LED	ITO/AlN (10/20 nm)	5.2 (3.7% ↓)	−46.9	37.2 (8.6% ↑)	3.7×10^{-2}	95.0 at 365 nm
	100 nm thick ITO	5.4	−67.2	34.3	4.5×10^{-2}	88.7 at 385 nm

optimized to obtain the best performance for each emission wavelength for reliable comparison. We then calculated the specific contact resistance (ρ_C) of the ITO/AlN TCEs and reference ITOs on p-(Al)GaN using the TLM plot (Figure S7), and found some reduction (or improvement) in the ρ_C of the

ITO/AlN TCEs when compared to those of the reference ITOs. The ρ_C values of each sample are summarized in Table 1.

Next, we investigated the optical transmittance of the ITO/AlN (10/20 nm) TCEs as a function of wavelength, and compared it with that of the reference ITO deposited on quartz
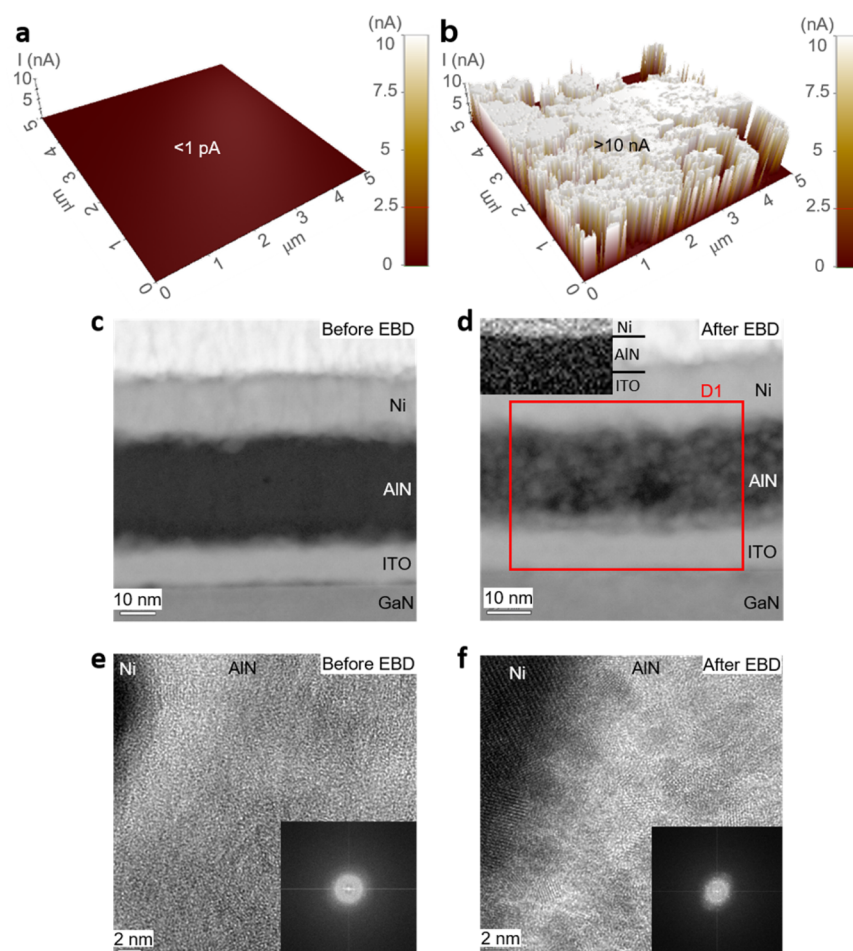
Figure 3. Structural and compositional analyses of the conducting filament formed in the AlN layers. C-AFM images taken for the AlN top layer (a) before and (b) after the EBD at 1 V with a compliance current of 10 nA. The current level is distinguished by the color scale bar displayed next to the C-AFM images. A HAADF-STEM image of Ni/AlN/ITO/p-GaN layers obtained under (c) before and (d) after the EBD. Scale bar: 10 nm. Ni−K EELS edge spectra are extracted from the D1 (inset of d). Corresponding position of D1 in the HAADF-STEM image is indicated by a solid red line in d. Typical HR-TEM images were taken of Ni/AlN layers (e) before and (f) after the EBD. Scale bar: 2 nm. Fast Fourier transformed micrographs of the high-resolution images are shown in the inset of e and f.

substrates (Figure 2e). The transmittance of ITO/AlN TCE was much higher compared with that of the reference ITOs, and the transmittance of the ITO/AlN TCEs was over 95% even at 365 nm. Figure 2f shows the photographs taken for a white background under the ITO/AlN TCEs and reference ITOs. On comparing, the white background under the ITO/AlN TCEs appears more clearly than that under the reference thick ITOs (thickness of 60, 110 nm) due to its high optical transmittance, even with naked eyes. The transmittance values in each sample are summarized for comparison, in Table 1.

We examined the rupture and formation of the CFs in the ITO/AlN layers before and after the EBD using conductive-atomic force microscopy (C-AFM), high-angle annular dark-field (HAADF) scanning transmission electron microscopy (STEM), and high-resolution TEM (HR-TEM) to understand the conduction mechanism in the TCE film. To explain the ohmic mechanism of the ITO/AlN TCEs on p-(Al)GaN after the EBD, we further analyzed one of the LED samples (p-GaN terminated 385 nm LED) before and after the EBD, particularly at the interface between p-GaN and ITO/AlN TCE, using secondary ion mass spectroscopy (SIMS), X-ray diffraction (XRD), and X-ray photoelectron spectroscopy (XPS).

We measured C-AFM images at 1 V from the ITO/AlN (10/20 nm) TCE before and after the EBD as shown in Figure 3a, b, respectively, after removing the Cr/Ni pad (Figure S8). The result indicates that the CFs (or current injection path) are formed stably in the ITO/AlN TCE after the EBD. Note that the origin of the CFs has been identified as either oxygen or nitrogen vacancies under bias applications[32,33] or conducting bridges consisting of ionized metals.[34]

In addition, we measured HAADF-STEM images (Figure 3c, d) for the samples before and after the EBD, respectively. The result of the measurement indicates that a kind of conducting channel is evenly formed across the entire region of the AlN layer after the EBD (Figure 3d), when compared to the image before the EBD (Figure 3c). For qualitative analyses of conducting channels in the ITO/AlN layer, we studied Ni−K, Al−K, and N−K edge electron energy loss spectroscopy (EELS) spectra taken at the local region labeled D1, as indicated in the inset of Figure 3d and Figure S9. Ni−K EELS edge spectra exhibit the presence of nickel after the EBD in the AlN layer as well as ITO because of the migration of nickel ions (inset of Figure 3d), whereas aluminum and nitrogen intensities are hardly detectable in the ITO layer (Figure S9). Consequently, the conducting channels
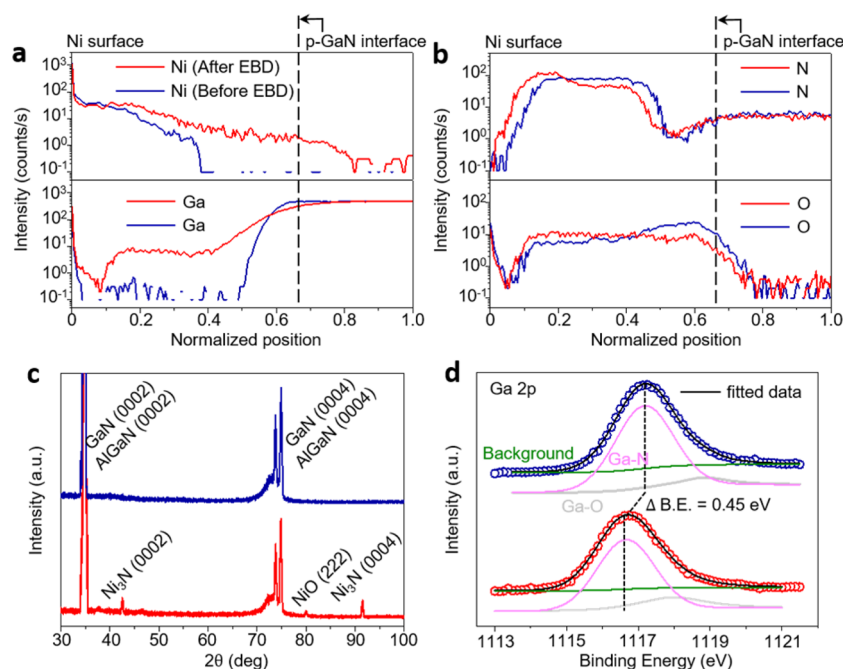
Figure 4. Ohmic mechanisms for the p-GaN terminated 385 nm LEDs with ITO/AlN TCEs. SIMS depth profiles of the (a) Ni, Ga, (b) N, and O before (blue line) and after (red line) the EBD. (c) XRD spectra measured at the p-GaN surface before (blue line) and after (red line) the EBD. (d) XPS spectra measured for the Ga 2p core level of the p-GaN surface before (blue open circles) and after (red open circles) the EBD.

formed in the AlN layers after the EBD are thought to consist of nickel ions.

We then investigated the change in the structure of the AlN layer by analyzing HR-TEM images before (Figure 3e) and after (Figure 3f) the EBD. By comparison, it is clearly observed that some grains are partially formed in the AlN layer after the EBD (Figure 3f). These grains are thought to result from local crystallization driven by nickel ion diffusion. The fast Fourier transform micrographs of the HR-TEM images also support the same conclusion. Compared to the sample before the EBD (inset of Figure 3e), brighter diffraction spots are observed for the sample after the EBD (inset of Figure 3f).

Next, we investigated the change in the relative atomic concentrations of Ga, Ni, N, O, Al, Cr, In, and Sn using SIMS, before and after the EBD (Figure 4a, b and Figure S10). Here, Ni atoms in the Ni pad are diffused toward p-GaN, whereas Ga atoms in p-GaN are also diffused toward Ni, leading to Ga vacancies (serving as acceptor) in the p-GaN contact layers after the EBD (Figure 4a). Then, to figure out what happened at the interface between the ITO/AlN and p-GaN layers, we analyzed the p-GaN surface again after removing the ITO/AlN layer using XRD and XPS. Figure 4c shows the XRD spectra measured for the p-GaN terminated 385 nm LED before and after the EBD. Before the EBD, only peaks related to GaN and AlGaN was detected; however, after EBD, several peaks related to Ni_3N and NiO were detected along with GaN- and AlGaN-related peaks.[35] In addition, the peak intensity of GaN and AlGaN was slightly reduced after the EBD. This result indicates that the Ni atoms are diffused into the AlN or ITO layer to form the Ni_3N and NiO located at the p-GaN surface during the EBD process.

Similar results were observed in the XPS analysis of the p-GaN terminated 385 nm wafer structure performed before and after the EBD process. The evidence of the in-diffused Ni atoms after the EBD process is clearly shown by the Ni 2p peaks related to the various binding energies of Ni ions,[36] whereas no such Ni 2p peaks were found before the EBD process (Figure S11).

Generally, Ni compounds such as Ni_3N, NiO are known to improve the ohmic behavior of p-GaN by increasing the effective carrier concentration near the surface.[35]

Figure 4d shows the XPS Ga 2p core level spectra obtained for the same sample before and after EBD. The XPS core-level peak fittings were performed using a Shirley-type background and Lorentzian-Doniac-Sunsic curves convoluted with a Gaussian profile. The Ga 2p core levels are composed of the Ga−N and Ga−O bonds. The Ga 2p core level of the sample after the EBD shifts toward the lower binding energy side by ∼0.45 eV compared to that of the sample measured before the EBD. This result implies that the EBD shifts the surface Fermi level toward the valence band edge, eventually reducing the band bending of p-GaN. This blue shift indicates a lowering of the Schottky barrier height (SBH).[37] On the basis of these extensive analyses and findings, we conclude that the reduced contact resistance of the ITO/AlN TCE on p-GaN might have resulted from the increase in Ga vacancies in the p-GaN contact layers and the decrease in the SBH between the ITO/AlN TCE and p-GaN, after the EBD.

Finally, we measured the device performance, including the I−V curves, light output power−current (L−I), electroluminescence (EL) spectra, and light emission images for the three LEDs with the ITO/AlN (10/20 nm) TCEs and two reference ITOs (10 nm, 60−110 nm) in each set of the four types of LEDs (Figure 5).

Figure 5a, e, i shows the L−I−V characteristic curves (Figure 5a), EL spectra versus wavelength and reverse leakage currents at −10 V (Figure 5e), and light emission images (Figure 5i) of the p-GaN terminated 450 nm LEDs with the ITO/AlN (10/20 nm) TCEs and reference ITOs (60 nm, 10 nm) TCEs under low and high current injection for comparison. In this case, we observed little difference in the electrical properties of both LEDs with ITO/AlN TCEs and reference ITO (60 nm). This is because the 60 nm thick ITOs were fully optimized for 450 nm GaN LEDs, which indicates that our proposed ohmic method is at least as
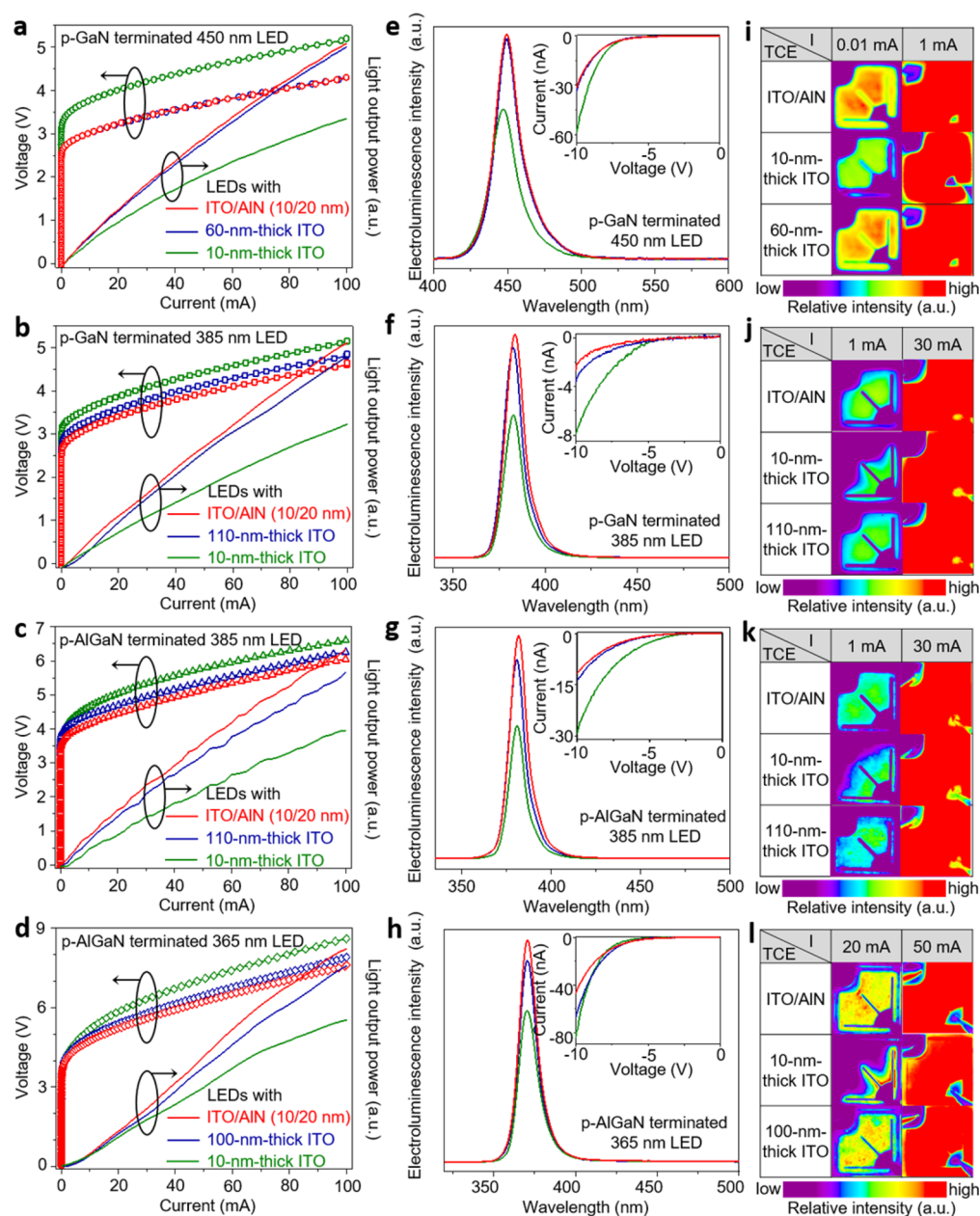
Figure 5. Electrical and optical characteristics and light-emission images of LEDs. Typical light-output power−current−voltage characteristics of (Al)GaN LEDs with ITO/AlN TCEs after the EBD (red open symbols), 60/110/100 nm thick ITO layers (blue open symbols) and 10 nm thick ITO layers (green open symbols) deposited on (a) p-GaN terminated 450 nm wafer, (b) p-GaN terminated 385 nm wafer, (c) p-AlGaN terminated 385 nm wafer, and (d) p-AlGaN terminated 365 nm wafer. Electroluminescence spectra versus wavelength and reverse leakage currents (inset) measured for (Al)GaN LEDs with ITO/AlN TCEs after the EBD (red line), 60/110/100 nm thick ITOs (blue line), and 10 nm thick ITOs (green line) deposited on (e) p-GaN terminated 450 nm wafer, (f) p-GaN terminated 385 nm wafer, (g) p-AlGaN terminated 385 nm wafer, and (h) p-AlGaN terminated 365 nm wafer, respectively. Microscopic light emission photographs measured at different currents for (Al)GaN LEDs with ITO/AlN TCEs after the EBD, 60/110/100 nm thick ITOs, and 100 nm thick ITOs deposited on (i) p-GaN terminated 450 nm wafer, (j) p-GaN terminated 385 nm wafer, (k) p-AlGaN terminated 385 nm wafer, and (l) p-AlGaN terminated 365 nm wafer. The linear color scale for intensity distribution is given directly below the photograph.

good as the conventional one. In the optical properties, a slight improvement was observed in the light output power and EL intensity for the ITO/AlN TCE-based LEDs, probably because of its higher transmittance at 450 nm (97.8%) compared with that of the 60 nm thick ITO (92.7%).

Figures 5b, f, and j show the L−I−V characteristic curves (Figure 5b), EL spectra versus wavelength and reverse leakage currents at −10 V (Figure 5f), and light emission images (Figure 5j) of the p-GaN terminated 385 nm LEDs with ITO/AlN (10/

20 nm) TCEs and ITOs (110 nm, 10 nm) TCEs under low and high current injection for comparison. In the I−V curves, we observed a lower forward voltage, by 4.2%, and a lower reverse leakage current, by 27.8%, in the LEDs with ITO/AlN TCEs when compared to the LEDs with 110 nm thick reference ITOs. We also observed a higher light output power, by 4.7%, for the LEDs with ITO/AlN TCEs. These improvements are attributed to the enhanced current injection and spreading effect as well as higher transmittance using ITO/AlN TCEs. To evaluate the

current injection and spreading effect, we measured the light emission images from the LEDs with ITO/AlN (10/20 nm) TCEs, 110 nm thick ITOs, and 10 nm thick ITOs; we observed the brightest light emission from the LED with ITO/AlN TCE at 1 mA and 30 mA, respectively. Not shown here, the sheet resistance of a 10 nm thick ITO layer was reduced from 1201.8 to 93.8 $\Omega/\square$ after EBD, probably owing to the CFs, generally formed in a pyramidal (or branch-like) from the metal to p-(Al)GaN across the AlN/ITO film.[38,39] These CFs not only provide conducting channels for current injection but also enhance the current spreading effect, particularly via ITO buffer layers, over the ITO/AlN TCE. The EBD via ITO buffer layers can also help to produce the CFs uniformly over the film (because the conductivity of ITO is much greater than that of p-(Al)GaN), enhancing the current spreading effect as well.

Figure 5c, g, and k shows the $L-I-V$ characteristic curves (Figure 5c), EL spectra versus wavelength and reverse leakage currents at −10 V (Figure 5g), and light emission images (Figure 5k) of the p-AlGaN terminated 385 nm LEDs with ITO/AlN (10/20 nm) and ITO (110 nm, 10 nm) TCEs under low and high current injection for comparison. In the I−V curves (Figure 5c, g), we observed a lower forward voltage, by 6.4%, and a lower reverse leakage current, by 16.8%, for the LEDs with ITO/AlN TCEs when compared to the LEDs with 110 nm thick reference ITOs, as is the case for the LED with the p-GaN terminated 385 nm wafer. We also observed a higher light output power, by 13%, for the LEDs with ITO/AlN TCEs against the LEDs with 110 nm thick ITOs. We measured the light emission images for the LEDs with ITO/AlN (10/20 nm) TCEs, 110 nm thick ITOs, and 10 nm thick ITOs; we observed the brightest light emission from the LEDs with ITO/AlN TCEs at 1 and 30 mA, respectively. Further improvements in the light output power from the p-AlGaN terminated 385 nm LEDs, rather than that from the p-GaN terminated 385 nm LED, even with the ITO/AlN TCEs, might be due to the lower light absorption tails incurred in the p-AlGaN contact layers.

Figure 5d, h, l shows the $L-I-V$ characteristic curves (Figure 5d), EL spectra versus wavelength and reverse leakage currents at −10 V (Figure 5h), and light emission images (Figure 5l) taken for the p-AlGaN terminated 365 nm LEDs with ITO/AlN (10/20 nm) and ITO (100 nm, 10 nm) TCEs. We observed a lower forward voltage, by 3.7%, and a reverse leakage current, by 30.2%, for the LEDs with ITO/AlN TCEs when compared to the LEDs with ITOs. We also observed a higher light output power, by 8.6%, for the LEDs with ITO/AlN TCEs against the LEDs with ITOs. We measured the light emission images for the LEDs with ITO/AlN (10/20 nm) TCEs, 100 nm thick ITOs, and 10 nm thick ITOs; we observed the brightest light emission from the LEDs with ITO/AlN TCEs at 20 mA and 50 mA, respectively. Detailed values for the LED performance (e.g., forward voltage (V_F), reverse leakage current (I_L), light output power (P_O), specific contact resistance (ρ_C), and transmittance) of the four types of LEDs, each type with a set of three LEDs with ITO/AlN TCE, 10 nm thick ITO, and 60−110 nm thick ITO, are summarized in Table 1.

Finally, we investigated the reliability of the LEDs with AlN/ITO TCEs. We first obtained the chip-to-chip uniformity statistical data in both EL intensities and forward voltages for 50 different p-GaN terminated 385 nm LEDs with ITO/AlN TCEs after EBD, 110 nm thick ITO, and 10 nm thick ITO layers as p-type electrodes, respectively, as shown in Figure S12. These results exhibit that LEDs with ITO/AlN TCEs have more uniform device performance when compared to those with ITO

electrodes. In addition, we measured the EL intensities and their emission images over time for both 385 and 365 nm (Al)GaN LEDs with ITO/AlN TCEs after EBD, as shown in Figure S12. These results indicate that the performance of LEDs with proposed ITO/AlN TCEs are quite stable over time.

3. CONCLUSION

In summary, we proposed a new concept of G-TCEs using the ITO/AlN (10/20 nm) thin film with high transmittance and low contact resistance, and successfully demonstrated its validity at the device level by applying them to nitride-based VIS-to-UV LEDs (365−450 nm). In case of the TCE, by introducing thin ITO buffer layers between the AlN and p-(Al)GaN layers, we could eradicate the concern regarding the electrical damage in the MQW during the EBD process, or nonuniform light emission due to poor current spreading. Regarding ohmic characteristics, we found that the ρ_C values of the ITO/AlN TCEs are lower than those of the reference ITOs for all samples. To explain this result, we investigated the ohmic mechanism using the SIMS, XRD, XPS, and C-AFM, and concluded that the reduction in the SBH due to the formation of Ni_3N or NiO at the interface between the ITO/AlN TCE and p-(Al)GaN, and the creation of Ga vacancies (serving as acceptors) in the p-(Al)GaN contact layers during the EBD and thermal annealing process are responsible for the improvement in the contact properties. The optical transmittance of the ITO/AlN TCE (95.0−97.8%) was much higher than that of the ITO structures (88.7−92.7%). Finally, we applied the ITO/AlN TCEs to the four types of (Al)GaN LEDs, and compared them with the ITO-based LEDs. Overall, LEDs with ITO/AlN TCEs exhibited much higher light output powers and lower forward voltages than those exhibited by the ITO-LEDs at 365−450 nm wavelengths. In particular, the p-AlGaN terminated near-UV LEDs exhibited better optical properties than the p-GaN terminated ones due to reduced light absorption in the p-AlGaN contact layers. This result indicates that forming a direct contact to p-AlGaN is important in order to improve the efficiency of UV LEDs, particularly for deep UV LEDs (200−280 nm). This result indicates that forming a direct contact to p-AlGaN is important in order to improve the efficiency of UV LEDs, particularly for deep UV LEDs (200−280 nm). We believe that our G-TCE can bring a technical breakthrough in many optoelectronic areas including high-power solid-state lighting, display, solar cells, and deep UV LEDs, by providing greater freedom and better performance for ohmic contacts to WB semiconductors.

4. EXPERIMENTAL SECTION

Fabrication of (Al)GaN-Based Lateral LEDs. We prepared four types of (Al)GaN LED wafers (p-GaN terminated 450 nm wafer, p-GaN terminated 385 nm wafer, p-$Al_{0.05}Ga_{0.95}N$ terminated 385 nm wafer, and p-$Al_{0.1}Ga_{0.9}N$ terminated 365 nm wafer), and fabricated three LEDs with different TCEs−ITO/AlN (10/20 nm) and two reference ITOs (10 nm, 60−110 nm)—in each wafer for comparison. All wafers were grown by metal−organic chemical vapor deposition on c-plane sapphire substrates. Detailed information on the epilayer structures is presented in the Scheme S1. For LED fabrication, standard photolithography and inductively coupled plasma reactive-ion etching were used to form isolated fan-shaped mesa structures in all the LED samples. The samples were then cleaned with a piranha solution (1:1 mixture of H_2SO_4:H_2O_2) for 10 min to remove the organic residues from the substrates. Next, they were cleaned in 30:1 buffered oxide etchants for 10 min to remove the surface oxide. Then, 10 nm thick ITO buffer layers with isolated mesa structures were deposited using electron-beam (E-beam) evaporation, and the samples were annealed using rapid thermal

processes (RTP) at 550 °C for 60 s. Next, 20 nm thick AlN thin films with isolated mesa structures were deposited on the ITO buffer layers using a radio frequency (RF) magnetron sputtering system in Ar−N$_2$ gas environments at a base pressure of ∼2 × 10^{-7} Torr and a working pressure of ∼3 × 10^{-3} Torr. The sample was further annealed using RTP in N$_2$ gas environment at 600 °C for 30 s for recrystallization. Subsequently, a dot-shaped Cr/Ni (2/15 nm) pad for the EBD was deposited by E-beam evaporation, and the EBD process was performed for the formation of the CFs in the ITO/AlN layer by applying voltages between the Cr/Ni dot and ITO buffer layers. Finally, Cr/Ni/Au was deposited using E-beam evaporation to form the p- and n-type electrodes. The chip size was 390 μm × 390 μm (Figure S13). For comparison, (Al)GaN LEDs with 10, 60, 100, and 110 nm thick ITO layers and Cr/Ni/Au electrodes were also fabricated using the same wafer and the same fabrication condition.

Electrical and Optical Characterizations. First, we used the TLM to evaluate the ohmic contact properties of the proposed ITO/AlN TCEs deposited on the p-(Al)GaN layers. To fabricate the TLM patterns, a 10 nm thick ITO, a 20 nm thick AlN, and 2/15 nm thick Cr/Ni layers were deposited with varied spacings from 5−25 μm, after which the EBD processes were performed between the ITO buffer and Ni pad layers under the same condition as LED fabrication. Then, Cr/Ni/Au was deposited as the electrode under the same condition. For comparison, the TLM patterns consisting of 10, 60, 110, and 100 nm thick ITO layers and Cr/Ni/Au electrodes were also fabricated using the same wafer under the same condition. The I−V curves in each TLM pattern were then measured using a Keithley 4200 semiconductor parameter analyzer.

Next, to evaluate the transmittance of the proposed ITO/AlN TCEs, we deposited 10 nm thick ITO and 20 nm thick AlN layers on the quartz substrates using E-beam evaporation and RF sputtering system, respectively, using the same condition as for LED fabrication. For comparison, we also deposited 10, 60, 110, and 100 nm thick ITO layers on the quartz substrates using E-beam evaporation under the same condition. We then measured the transmittance of the samples as a function of wavelength using the Lambda 35 UV/vis spectrometer with an operating wavelength range of 190−1100 nm.

Finally, we measured the performance of each LED (i.e., forward voltages, reverse leakage currents, light output power, EL, and emission images) using an LED measurement system (PLATO, EtaMax Co., Ltd. with a Keithley 2400 source measure unit) (Figure S13). For more insight, the light output power and EL intensity of each LED were measured from the top side of the LED using a Si photodiode connected to the optical power meter. The light emission images were then taken from the surface of the LED chips using a photoemission microscope.

CAFM Measurement and Sample Preparation. Current mapping on the top of the AlN layer was achieved using a Cr/Pt−Ir coated Si probe (Park systems, CONTSCPt) in contact mode with contact forces of ∼4−8 nN, a scan rate of 1.5 Hz, and a sample bias of 1.0 V after removing the Cr/Ni layers using the nichrome etchant (Sigma-Aldrich) (Figure S8). Currents were then collected through the CAFM probe using a variable gain enhanced current amplifier (measurement current compliance: 10 nA).

HAADF-STEM, HR-TEM, and EELS Analyses. The Cs-corrected STEM, HR-TEM, and EELS analyses were performed using a field-emission TEM with a Cs corrector (JEM-2100F, JEOL) at an accelerating voltage of 200 kV. The aberration-corrected STEM image have a convergence angle of 24 mrad. The inner and outer angle of the HAADF detector was 173 and 227 mrad, respectively. In addition, the energy dispersion and collection angles for EELS were 0.7 eV/ch and 35 mrad, respectively.

SIMS Analysis and Sample Preparation. To investigate the chemical depth profiles of the ITO/AlN TCE on p-(Al)GaN before and after the EBD, samples were measured using TOF-SIMS (TOF-SIMS 5, ION TOF) equipped with a liquid bismuth ion source and pulse electron flooding (Figure S10). During analysis and sputtering, the targets were bombarded by 25 kV bismuth beams with a pulsed primary ion current of 1.0 pA for analysis and 1 keV cesium beams with a pulsed primary ion of 12.0 nA for sputtering. In analysis, positive polarities were used for Ga (Ga+), Ni (Ni+), Al (Al+), Cr (Cr+), In (In+), and Sn (Sn +), and negative polarities were used for N (NH−), O (18O−). The analysis and sputtering area were 50 μm × 50 and 300 μm × 300 μm, respectively.

XRD and XPS Analyses and Sample Preparation. Samples for XRD and XPS experiments were continued on the surface of p-GaN layers after removing the ITO layers using the hydrochloric acid (HCl) (Figure S11). XRD experiments were performed on an automated multipurpose X-ray diffractometer system (SmartLab, Rigaku) using Cu Kα radiation. Each sample was adhered to a stainless steel sample holder and aligned with the X-ray beam. The voltage and current were 45 kV and 200 mA, respectively. The 2θ scan range was 30−110°, the scanning resolution was 0.01° per step, and the scanning speed was 1°/min. XPS experiments were performed using a 24.1 W monochromatized Al Kα radiation source (X-tool, ULVAC-PHI), where the takeoff angle was 45°. The scan area was 100 μm × 100 μm, and the binding energy ranges of the narrow-scan spectra for Ni 2p and Ga 2p core level were from 894 to 844 eV and from 1113 to 1122 eV, respectively, using 0.125 eV/step. To analyze XPS spectra, we used a nonlinear least-squares curve fitting program (XPSPEAK 4.1 software) with mixed Gauss−Lorentz product function and Shirley background.

■ ASSOCIATED CONTENT

Ⓢ Supporting Information

The Supporting Information is available free of charge on the ACS Publications website at DOI: 10.1021/acsami.6b12767.

Schematic of the detailed epilayer structures of four AlGaN LEDs (Scheme S1) and schematic of fabrication process for lateral-type LEDs with ITO/AlN TCEs (Scheme S2); issues related to MQW damage during the EBD or poor current spreading observed for AlGaN LED with AlN TCE, without ITO buffer layer (Figure S1); thickness optimization of ITO buffer layers (Figure S2); EBD behavior of various wide-bandgap thin films (Figure S3); film thickness of ITO/AlN (10/20 nm) TCE measured by AFM (Figure S4); EBD behavior of ITO/AlN TCEs deposited on different epi-wafers (Figure S5); ohmic behavior of the optimal ITOs deposited on the four (Al)GaN LEDs (Figure S6); ohmic behavior of the ITO/AlN TCEs after EBD and optimal ITOs on (Al)GaN wafers (Figure S7); measurement setup for C-AFM imaging (Figure S8); structural and compositional analysis of the conducting filament formed in the AlN layers (Figure S9); SIMS data for whole ions before and after EBD (Figure S10); XPS and XRD measurement before and after EBD (Figure S11); reliability data of LEDs with the ITO/AlN TCEs after EBD and optimal ITOs on (Al)GaN wafers (Figure S12); photograph of the LED samples on the 2 in. wafers (Figure S13) (PDF)

■ AUTHOR INFORMATION

Corresponding Author

*E-mail: tgkim1@korea.ac.kr. Phone: +82-2-3290-3255. Fax: +82-2-924-5119.

ORCID ⦿

Tae Geun Kim: 0000-0001-6211-1134

Notes

The authors declare no competing financial interest.

■ ACKNOWLEDGMENTS

■ REFERENCES

(1) Park, T. Y.; Choi, Y. S.; Kang, J. W.; Jeong, J. H.; Park, S. J.; Jeon, D. M.; Kim, J. W.; Kim, Y. C. Enhanced Optical Power and Low Forward Voltage of GaN-Based Light-Emitting Diodes with Ga-Doped ZnO Transparent Conducting Layer. *Appl. Phys. Lett.* **2010**, *96*, 051124.

(2) Kim, B. J.; Lee, C.; Jung, Y.; Baik, K. H.; Mastro, M. A.; Hite, J. K.; Eddy, C. R., Jr.; Kim, J. Large-Area Transparent Conductive Few-Layer Graphene Electrode in GaN-Based Ultra-Violet Light-Emitting Diodes. *Appl. Phys. Lett.* **2011**, *99*, 143101.

(3) Chae, D. J.; Kim, D. Y.; Kim, T. G.; Sung, Y. M.; Kim, M. D. AlGaN-Based Ultraviolet Light-Emitting Diodes using Fluorine-Doped Indium Tin Oxide Electrodes. *Appl. Phys. Lett.* **2012**, *100*, 081110.

(4) Pang, S.; Hernandez, Y.; Feng, X.; Müllen, K. Graphene as Transparent Electrode Material for Organic Electronics. *Adv. Mater.* **2011**, *23*, 2779−2795.

(5) Han, T. H.; Lee, Y.; Choi, M. R.; Woo, S. H.; Bae, S. H.; Hong, B. H.; Ahn, J. H.; Lee, T. W. Extremely Efficient Flexible Organic Light-Emitting Diodes with Modified Graphene Anode. *Nat. Photonics* **2012**, *6*, 105−110.

(6) Kim, Y. H.; Lee, J.; Hofmann, S.; Gather, M. C.; Müller-Meskamp, L.; Leo, K. Achieving High Efficiency and Improved Stability in ITO-Free Transparent Organic Light-Emitting Diodes with Conductive Polymer Electrodes. *Adv. Funct. Mater.* **2013**, *23*, 3763−3769.

(7) Shi, X. B.; Qian, M.; Wang, Z. K.; Liao, L. S. Nano-Honeycomb Structured Transparent Electrode for Enhanced Light Extraction from Organic Light-Emitting Diodes. *Appl. Phys. Lett.* **2015**, *106*, 223301.

(8) Barnes, T. M.; Bergeson, J. D.; Tenent, R. C.; Larsen, B. A.; Teeter, G.; Jones, K. M.; Blackburn, J. L.; van de Lagemaat, J. van de Carbon Nanotube Network Electrodes Enabling Efficient Organic Solar Cells without a Hole Transport Layer. *Appl. Phys. Lett.* **2010**, *96*, 243309.

(9) Kim, Y. H.; Sachse, C.; Machala, M. L.; May, C.; Muller-Meskamp, L.; Leo, K. Highly Conductive PEDOT:PSS Electrode with Optimized Solvent and Thermal Post-Treatment for ITO-Free Organic Solar Cells. *Adv. Funct. Mater.* **2011**, *21*, 1076−1081.

(10) Lee, Y. Y.; Tu, K. H.; Yu, C. C.; Li, S. S.; Hwang, J. Y.; Lin, C. C.; Chen, K. H.; Chen, L. C.; Chen, H. L.; Chen, C. W. Top Laminated Graphene Electrode in a Semitransparent Polymer Solar Cell by Simultaneous Thermal Annealing/Releasing Method. *ACS Nano* **2011**, *5*, 6564−6570.

(11) Leem, D. S.; Edwards, A.; Faist, M.; Nelson, J.; Bradley, D. D. C.; de Mello, J. C. Efficient Organic Solar Cells with Solution-Processed Silver Nanowire Electrodes. *Adv. Mater.* **2011**, *23*, 4371−4375.

(12) Jin, H.; Tao, C.; Velusamy, M.; Aljada, M.; Zhang, Y.; Hambsch, M.; Burn, P. L.; Meredith, P. Efficient, Large Area ITO-and-PEDOT-Free Organic Solar Cell Sub-Modules. *Adv. Mater.* **2012**, *24*, 2572−2577.

(13) Zhao, G.; Wang, W.; Bae, T.-S.; Lee, S.-G.; Mun, C.; Lee, S.; Yu, H.; Lee, G.-H.; Song, M.; Yun, J. Stable Ultrathin Partially Oxidized Copper Film Electrode for Highly Efficient Flexible Solar Cells. *Nat. Commun.* **2015**, *6*, 8830.

(14) Wu, H.; Hu, L.; Rowell, M. W.; Kong, D.; Cha, J. J.; McDonough, J. R.; Zhu, J.; Yang, Y.; McGehee, M. D.; Cui, Y. Electrospun Metal Nanofiber Webs as High-Performance Transparent Electrode. *Nano Lett.* **2010**, *10*, 4242−4248.

(15) Ferry, V. E.; Polman, A.; Atwater, H. A. Modeling Light Trapping in Nanostructured Solar Cells. *ACS Nano* **2011**, *5*, 10055−10064.

(16) Kuang, P.; Park, J. M.; Leung, W.; Mahadevapuram, R. C.; Nalwa, K. S.; Kim, T. G.; Chaudhary, S.; Ho, K. M.; Constant, K. A New Architecture for Transparent Electrodes: Relieving the Trade-Off Between Electrical Conductivity and Optical Transmittance. *Adv. Mater.* **2011**, *23*, 2469−2473.

(17) Zhou, Y. H.; Fuentes-Hernandez, C.; Shim, J.; Meyer, J.; Giordano, A. J.; Li, H.; Winget, P.; Papadopoulos, T.; Cheun, H.; Kim, J.; Fenoll, M.; Dindar, A.; Haske, W.; Najafabadi, E.; Khan, T. M.; Sojoudi, H.; Barlow, S.; Graham, S.; Brédas, J. L.; Marder, S. R.; Kahn, A.; Kippelen, B. A Universal Method to Produce Low-Work Function Electrodes for Organic Electronics. *Science* **2012**, *336*, 327−332.

(18) De, S.; Higgins, T. M.; Lyons, P. E.; Doherty, E. M.; Nirmalraj, P. N.; Blau, W. J.; Boland, J. J.; Coleman, J. N. Silver Nanowire Networks as Flexible, Transparent, Conducting Films: Extremely High DC to Optical Conductivity Ratios. *ACS Nano* **2009**, *3*, 1767−1774.

(19) Rathmell, A. R.; Bergin, S. M.; Hua, Y. L.; Li, Z. Y.; Wiley, B. J. The Growth Mechanism of Copper Nanowires and Their Properties in Flexible, Transparent Conducting Films. *Adv. Mater.* **2010**, *22*, 3558−3563.

(20) Garnett, E. C.; Cai, W.; Cha, J. J.; Mahmood, F.; Connor, S. T.; Christoforo, M. G.; Cui, Y.; McGehee, M. D.; Brongersma, M. L. Self-Limited Plasmonic Welding of Silver Nanowire Junctions. *Nat. Mater.* **2012**, *11*, 241−249.

(21) Hsu, P. C.; Wang, S.; Wu, H.; Narasimhan, V. K.; Kong, D.; Lee, H. R.; Cui, Y. Performance Enhancement of Metal Nanowire Transparent Conducting Electrodes by Mesoscale Metal Wires. *Nat. Commun.* **2013**, *4*, 2522.

(22) Lee, J.-Y.; Connor, S. T.; Cui, Y.; Peumans, P. Solution-Processed Metal Nanowire Mesh Transparent Electrodes. *Nano Lett.* **2008**, *8*, 689−692.

(23) Jang, H. Y.; Lee, S. K.; Cho, S. H.; Ahn, J. H.; Park, S. Fabrication of Metallic Nanomesh: Pt Nano-Mesh as a Proof of Concept for Stretchable and Transparent Electrodes. *Chem. Mater.* **2013**, *25*, 3535−3538.

(24) Guo, C. F.; Sun, T.; Liu, Q.; Suo, Z.; Ren, Z. Highly Stretchable and Transparent Nanomesh Electrodes Made by Grain Boundary Lithography. *Nat. Commun.* **2014**, *5*, 3121.

(25) Kim, K. S.; Zhao, Y.; Jang, H.; Lee, S. Y.; Kim, J. M.; Kim, K. S.; Ahn, J. H.; Kim, P.; Choi, J. Y.; Hong, B. H. Large-Scale Pattern Growth of Graphene Films for Stretchable Transparent Electrodes. *Nature* **2009**, *457*, 706−710.

(26) Gomez de Arco, L.; Zhang, Y.; Schlenker, C. W.; Ryu, K.; Thompson, M. E.; Zhou, C. Continuous, Highly Flexible, and Transparent Graphene Films by Chemical Vapor Deposition for Organic Photovoltaics. *ACS Nano* **2010**, *4*, 2865−2873.

(27) Bae, S.; Kim, H.; Lee, Y.; Xu, X.; Park, J. S.; Zheng, Y.; Balakrishnan, J.; Lei, T.; Kim, H. R.; Song, Y. I.; Kim, Y. J.; Kim, K. S.; Ozyilmaz, B.; Ahn, J. H.; Hong, B. H.; Iijima, S. Roll-to-Roll Production of 30-Inch Graphene Films for Transparent Electrodes. *Nat. Nanotechnol.* **2010**, *5*, 574−578.

(28) Wu, Z. C.; Chen, Z. H.; Du, X.; Logan, J. M.; Sippel, J.; Nikolou, M.; Kamaras, K.; Reynolds, J. R.; Tanner, D. B.; Hebard, A. F.; Rinzler, A. G. Transparent, Conductive Carbon Nanotube Films. *Science* **2004**, *305*, 1273−1276.

(29) Hu, L.; Hecht, D. S.; Grüner, G. Percolation in Transparent and Conducting Carbon Nanotube Networks. *Nano Lett.* **2004**, *4*, 2513−2517.

(30) Lee, D. J.; Kim, H. M.; Kwon, J. Y.; Choi, H.; Kim, S. H.; Kim, K. B. Structural and Electrical Properties of Atomic Layer Deposited Al-Doped ZnO Films. *Adv. Funct. Mater.* **2011**, *21*, 448−455.

(31) Vosgueritchian, M.; Lipomi, D. J.; Bao, Z. Highly Conductive and Transparent PEDOT:PSS Films with a Fluorosurfactant for Stretchable and Flexible Transparent Electrodes. *Adv. Funct. Mater.* **2012**, *22*, 421−428.

(32) Kim, H. D.; An, H. M.; Kim, K. H.; Kim, S. J.; Kim, C. S.; Cho, J.; Schubert, E. F.; Kim, T. G. A Universal Method of Producing Transparent Electrodes Using Wide-Bandgap Materials. *Adv. Funct. Mater.* **2014**, *24*, 1575−1581.

(33) Wedig, A.; Luebben, M.; Cho, D. Y.; Moors, M.; Skaja, K.; Rana, V.; Hasegawa, T.; Adepalli, K. K.; Yildiz, B.; Waser, R.; Valov, I. Nanoscale Cation Motion in TaO$_x$, HfO$_x$ and TiO$_x$ Memristive Systems. *Nat. Nanotechnol.* **2016**, *11*, 67−74.

(34) Fujiwara, K.; Nemoto, T.; Rozenberg, M. J.; Nakamura, Y.; Takagi, H. Resistance Switching and Formation of a Conductive Bridge in Metal/Binary Oxide/Metal Structure for Memory Devices. *Jpn. J. Appl. Phys.* **2008**, *47*, 6266−6271.

(35) Hsu, C.-Y.; Lan, W.-H.; Wu, Y.-S. Thermal Annealing Effect Between Ni Film and Mg-Doped GaN Layer. *Jpn. J. Appl. Phys.* **2006**, *45*, 6256−6258.

(36) Tan, Z. A.; Zhang, W.; Qian, D.; Cui, C.; Xu, Q.; Li, L.; Li, S.; Li, Y. F. Solution-Processed Nickel Acetate as Hole Collection Layer for Polymer Solar Cells. *Phys. Chem. Chem. Phys.* **2012**, *14*, 14217−14223.

(37) Song, J. O.; Ha, J.-S.; Seong, T.-Y. Ohmic-Contact Technology for GaN-Based Light-Emitting Diodes: Role of P-Type Contact. *IEEE Trans. Electron Devices* **2010**, *57*, 42−59.

(38) Park, G.-S.; Li, X.-S.; Kim, D.-C.; Jung, R.-J.; Lee, M. J.; Seo, S. Observation of Electric-Field Induced Ni Filament Channels in Polycrystalline NiO$_x$ Film. *Appl. Phys. Lett.* **2007**, *91*, 222103.

(39) Ninomiya, T.; Takagi, T.; Wei, Z.; Muraoka, S.; Yasuhara, R.; Katayama, K.; Ikeda, Y.; Kawai, K.; Kato, Y.; Kawashima, Y.; Ito, S.; Mikawa, T.; Shimakawa, K.; Aono, K. Conductive Filament Scaling of TaO$_x$ Bipolar ReRAM for Long Retention with Low Current Operation. *Symp. VLSI Technol., Dig. Technol. Pap.* **2012**, 73−74.